ACCSCIENCE PUBLISHING

International Journal of Bioprinting

RESEARCH ARTICLE

Hydroxyapatite/BMP-2–mineralized decellularized amniotic membrane scaffolds for orbital defect repair

Bing Qin[1†], Yi Wang[2,3†], Yiyi Chen[4], Yabo Shi[1], and Wei Liu[1*]

[1]Department of Ophthalmology, The Affiliated Suqian First People's Hospital of Nanjing Medical University, Suqian, Jiangsu, China

[2]Department of Ophthalmology, Peking University Third Hospital, Beijing, China

[3]Beijing Key Laboratory of Restoration of Damaged Ocular Nerve, Peking University Third Hospital, Beijing, China

[4]Department of Ophthalmology, The People's Hospital of Yangzhong City, Affiliated Hospital of Yangzhou University, Zhenjiang 212200, Jiangsu, China

Abstract

Orbital wall fractures often result in midfacial deformities characterized by herniation of orbital adipose and soft tissues into the maxillary sinus, potentially causing endophthalmitis or subbulbar inflammation. However, current orbital reconstruction materials face critical limitations, including inadequate osteogenic capacity and poor osseointegration, predisposing implants to displacement, immune rejection, and infection. To overcome these challenges, we fabricated a three-dimensional (3D)-printed scaffold based on hydroxyapatite/bone morphogenetic protein-2–mineralized decellularized amniotic membrane for orbital defect repair. By precisely modulating the material composition and leveraging advanced 3D printing techniques, we achieved simultaneous control over the scaffold's physicochemical properties and biological activity. The resulting constructs feature optimized macro- and micro-architectures. This study establishes a novel strategy for orbital reconstruction, addressing both bone volume restoration and functional regeneration, offering a transformative approach for personalized craniofacial repair.

Keywords: 3D printing; Acellular matrix; BMP-2; Composite scaffolds; Orbital reconstruction

†The authors contributed equally to this work.

***Corresponding author:**
Wei Liu (m13813182298@163.com)

Citation: Qin B, Wang Y, Chen Y, Shi Y, Liu W. Hydroxyapatite/BMP-2–mineralized decellularized amniotic membrane scaffolds for orbital defect repair. *Int J Bioprint*. 2026;12(1):283-301. doi: 10.36922/IJB025330336

Received: August 17, 2025
Revised: September 27, 2025
Accepted: October 11, 2025
Published online: October 14, 2025

1. Introduction

The orbital bone structure is particularly susceptible to fracture under external impact due to its thin structure, especially along the infraorbital wall. With the accelerated advancement of contemporary transportation and increased activities, the incidence of orbital fractures has demonstrated a discernible upward trajectory on an annual basis. Orbital fractures can lead to herniation and entrapment of orbital contents through the bone defect. In severe cases, prompt surgical intervention is necessary to achieve morphological repair and functional reconstruction. Clinically, the surgical approach of filling the orbital bone defect to support the infraorbital tissues and maintain the

normal position of the eyeball has been identified as an effective means of management.[1] However, the orbital wall is adjacent to the paranasal sinuses and has a relatively poor blood supply, with the defect area often covered by fibromucosal tissue, posing challenges for bone regeneration.[2] Therefore, bone graft materials should possess excellent osteoinductive activity to overcome the unfavorable conditions of local osteoblast deficiency, as well as good biodegradability and integration to guide new bone ingrowth rather than being isolated by fibrous tissue.

At present, the materials used in clinical orbital bone defect repair include traditional titanium mesh, high-density polyethylene, and autologous bone fragments. However, these materials have shortcomings in orbital bone defect repair.[3–7] First, non-resorbable materials are incapable of degrading *in vivo*, and their long-term presence as foreign bodies increases the risk of complications, such as displacement, rejection, and infection. Second, fibrous tissue is biologically inert and tends to become entangled, often leading to cyst formation. Third, the absence of osteoinductivity properties delays the regeneration of native bone, resulting in unsatisfactory repair of orbital bone defects. Moreover, existing materials prove inadequate for effective orbital bone reconstruction, as their biological and mechanical properties frequently fall short of clinical demands. Therefore, there is a pressing clinical need to develop novel materials and repair strategies to overcome the challenges associated with orbital bone defect repair and reconstruction, and to reduce the risks posed by traditional implant materials.

Human acellular amniotic membrane matrix (HAM) is a natural scaffold material derived from the collagenous extracellular matrix of the human placenta. It serves as a cost-effective and biocompatible alternative to other biomaterials. HAM expresses various growth factors and promotes neovascularization by stimulating epithelial cell proliferation and migration.[8,9] Although HAM exhibits inherent mechanical limitations, these can be effectively mitigated by forming composite materials, thereby improving its biomechanical properties. Studies have reported the application of HAM in reconstructing oral and maxillofacial defects, with evidence supporting its role in bone differentiation, repair, and regeneration.[10] To enhance both biological and mechanical performance, researchers have employed different strategies, including hydrogel fabrication, integration with electrospun layers, and surface coating.[11,12]

Hydroxyapatite (HAP), a pioneering material in porous orbital implants, received rapid approval from the United States (US) Food and Drug Administration and has been commercialized as the Bio-Eye sphere.[13] Composites of HAP with organic polymers not only mimic the composition of natural bone but also significantly improve the mechanical properties of scaffold materials.[14] Incorporating HAP into gel-based and pure HAM systems offers a promising approach to combine their advantages and develop biomaterials with superior mechanical performance.[15,16] However, simply mixing the two components cannot replicate the nanoscale architecture of mineralized collagen found in natural bone. In contrast, molecular template-mediated biomimetic mineralization allows controlled deposition of HAP crystals within and between collagen fibers, emulating the biological features of native bone and thus improving bone regeneration. Bone morphogenetic protein 2 (BMP-2) is recognized as one of the most potent osteoinductive factors, capable of recruiting bone marrow mesenchymal stem cells to sites of bone injury and promoting their proliferation and osteogenic differentiation.[17] Therefore, developing bioactive scaffold materials tailored to the local orbital microenvironment is of great significance for the repair of orbital bone defects.

To overcome the limitations of current orbital implant materials, this study developed a methacrylate-functionalized HAM (HAMMA), achieved by grafting methacrylic anhydride (MA) onto HAM. Decellularized HAM was mineralized with a HAP/BMP-2 coating via immersion in 10× simulated body fluid (SBF) supplemented with BMP-2. The composite scaffold (HAMMA/HAP/BMP-2) was fabricated using HAP particles, BMP-2, and HAMMA via three-dimensional (3D) printing combined with UV curing. The mechanical properties, swelling behavior, and degradation profile of the composite scaffolds were comprehensively evaluated. Furthermore, the potential of HAMMA/HAP/BMP-2 for orbital bone repair was assessed through *in vitro* cell studies and *in vivo* animal experiments.

2. Materials and methods

2.1. Preparation of HAMMA

The HAM was prepared from amniotic membranes obtained within 24 h following natural delivery and stored at 4°C. The study protocol was approved by the institutional review board. Briefly, the amniotic membrane was separated from the chorion via blunt dissection and washed three times with phosphate-buffered saline (PBS) to eliminate blood and cellular debris. Subsequently, the amniotic membrane was treated with a 0.1% ethylenediaminetetraacetic acid solution for 2 h at 37°C, followed by gentle scraping using a cell scraper to remove the epithelial layer. Following these treatments, the acellular amniotic membrane matrix was spread on a smooth and flat glass slab and air-dried overnight. The acellular amniotic membrane matrix was dissolved in 0.5 M acetic acid at a concentration of 10 mg/mL, and the pH was adjusted to a range of 8–9 using

NaOH. The mixture was then reacted with MA for 24 h. The resulting product was loaded into a dialysis bag with a molecular weight cutoff of 3500 Da and dialyzed for 2 days, followed by lyophilization to obtain spongy HAMMA.

2.2. Fabrication of HAMMA composite scaffolds

Kokubo's protocol was used to prepare 10× SBF. Recombinant human BMP-2 (10426-H01H, SinoBiological, China), at a concentration of 1% (w/v) of the total SBF volume, was added to the 10× SBF and gently vortexed to ensure thorough mixing while preventing aggregation. The 10% (w/v) spongy HAM was immersed in 10× SBF supplemented with 1% BMP-2 and incubated at 37°C under gentle agitation (50 rpm) for 7 days. The solution was replaced every 48 h to maintain ion saturation. The mineralized HAMA/HAP/BMP-2 was centrifuged, precipitated, and formed into a sol at 4°C. Then, 0.1% (w/v) lithium phenyl phosphate photoinitiator (LAP; L0290, TCI Shanghai, China) was added to the aforementioned mixture, and three scaffolds were constructed separately using 3D printing technology (SunP BioMaker 2, MilliporeSigma, US). Due to the physical filling and hydrogen bonding of HAP, the structure might be compromised once the printing process is complete. The scaffolds were subjected to photo-crosslinking under a UVLED point light source (395–480 nm, 10.5 mm curing tip; Ultradent Products, US) for 30 s—a step that could enhance the long-term stability of the composite scaffold.

2.3. Characterization of HAMMA composite scaffolds

The morphology and elemental distribution of the HAMMA composite scaffolds were characterized using scanning electron microscopy (SEM; Nova NanoSEM 450, Thermo Fisher Scientific, US). The crystalline phases were analyzed with an X-ray diffractometer (XRD; SmartLab-SE, Rigaku Corporation, Japan). The tensile properties of the scaffolds were measured on a universal testing machine (INSTRON 5943, Instron, US). The chemical composition of the HAP/BMP-2–mineralized scaffolds was examined using Fourier transform infrared spectroscopy (FTIR; IN10, Thermo Fisher Scientific, US) over the wavenumber range of 400–4000 cm^{-1}.

2.4. Degradation of HAMMA composite scaffolds

The HAMMA composite scaffolds were immersed in a PBS solution (10 mL, 9 mg/L, 37°C). After centrifugation at 7000 rpm for 10 min, the supernatant was collected and re-immersed in a fresh PBS solution (10 mL, 9 mg/L, 37°C). The experiment was continued for 28 days. Subsequently, the concentrations of BMP-2 in the supernatant were quantified using the human BMP-2 ELISA kit (E-EL-H0011, Elabscience, China). The degraded samples were centrifuged weekly, and the supernatant was discarded and replaced with fresh PBS. The mass loss of the composite scaffolds was calculated by deriving the mass difference, and the weight loss percentages of each sample were calculated based on Equation (1).

$$\text{Weight loss (\%)} = (W_1 - W_2)/W_1 \times 100\% \quad (1)$$

where W_2 is the mass of dry scaffolds at a specific time point, and W_1 is the initial weight of the dry scaffolds.

2.5. Swelling experiment of HAMMA composite scaffolds

The weight of HAMMA composite scaffolds was recorded as W_0. The scaffolds were then immersed in ultra-pure water for 0, 1, 2, 4, 6, 8, 12, or 24 h. Following the removal of the scaffolds, any surface moisture was removed by blotting with filter paper. The weight was subsequently recorded as W_1. The swelling ratio was calculated as follows:

$$\text{Swelling ratio (\%)} = (W_1 - W_0)/W_0 \times 100\% \quad (2)$$

where W_1 denotes the weight of the water-swollen gel at various time points and W_0 represents its final weight after the gelation process is complete.

2.6. Cell culture

The murine preosteoblast cell line MC3T3-E1 was obtained from the BeNa Culture Collection (China). The cells were cultured in alpha Eagle's minimal essential medium (Gibco, US) supplemented with 10% fetal bovine serum (Gibco, US) and 1% penicillin–streptomycin (Gibco, US), with the medium replaced every 3 days. For osteogenic differentiation induction, confluent MC3T3-E1 cells were stimulated with 10 nM dexamethasone (Sigma-Aldrich, US), 0.2 mM ascorbic acid (Sigma-Aldrich, US), and 10 mM β-glycerophosphate (Sigma-Aldrich, US). The induction medium was also refreshed every 3 days.

2.7. Cell compatibility

MC3T3-E1 cells were cultured with the HAMMA composite scaffolds for different time intervals (1, 3, or 5 d). Subsequently, cell counting kit 8 solution was added, followed by incubation in the dark at 37°C for 30 min. Absorbance was measured at 450 nm using the microplate reader to calculate cell viability. Meanwhile, the Calcein/PI Kit (Beyotime Biotechnology Institute, China) was prepared 30 min in advance and placed at room temperature. The staining working solution was prepared according to the instructions. After incubation at room temperature in the dark for 30 min, the samples were gently washed three times with PBS. Green fluorescence was imaged at the same location using a fluorescence microscope and documented. To examine cell morphology and spreading,

MC3T3-E1 cells were stained with TRITC phalloidin and 4',6-diamidino-2-phenylindole (DAPI) for cytoskeletal and nuclear visualization, respectively, and examined under an inverted fluorescence microscope (IX71, Olympus, Japan). A cell-free "scratch wound" was created on a monolayer of adherent cells, and cell migration ability was quantitatively assessed by monitoring cell movement into the scratched area over time using the same microscope system.

2.8. Alkaline phosphatase activity assay

After 7 days of differentiation and cultured with HAMMA composite scaffolds, MC3T3-E1 cells were washed three times with PBS and fixed with 4% paraformaldehyde for 30 min at room temperature, followed by washing with PBS. The fixed cells were treated with a 5-bromo-4-chloro-3-indolyl phosphate/nitroblue tetrazolium substrate kit (Beyotime Biotechnology Institute, China) for chromogenic detection of alkaline phosphatase (ALP) activity. The procedure was carried out in strict compliance with the manufacturer's protocol, and images were captured using an inverted microscope (Olympus IX71, Japan).

2.9. Alizarin red S staining

After 21 days of differentiation and culture with HAMMA composite scaffolds, MC3T3-E1 cells were washed three times with PBS and fixed in 4% paraformaldehyde for 30 min at room temperature. Following fixation, the cells were rinsed again with PBS. Subsequently, they were stained with 1% (w/v) alizarin red S solution for 15 min, followed by two additional PBS washes. Images were captured using an inverted microscope.

2.10. Western blot analysis

Cell lysates were prepared for Western blot analysis. Total protein was separated through sodium dodecyl sulfate–polyacrylamide gel electrophoresis. Following electrophoresis, the proteins were transferred onto polyvinylidene fluoride membranes. For immunodetection, the membranes were blocked with 5% non-fat dry milk for 12–16 h at 25°C. Primary antibodies (all purchased from Proteintech, US) against glyceraldehyde-3-phosphate dehydrogenase (GAPDH; 10494-1-AP), osteopontin (OPN; 25715-1-AP), Runx2 (20700-1-AP), and collagen type I (COL I; 14695-1-AP) were diluted at 1:1000. Detection was performed using horseradish peroxidase (HRP)-conjugated anti-mouse secondary antibodies (HRP-60004, Proteintech, US) diluted at 1:3000 in 5% non-fat dry milk prepared in Tris-buffered saline with Tween 20. Blots were visualized using enhanced chemiluminescence and a protein blot detection system.

2.11. RNA sequencing

MC3T3-E1 cells (3×10^6) cultivated with the composite scaffolds were treated with TRIzol reagent (Invitrogen, US) at 8 h after ultrasound treatment. The experiments were independently conducted three times for each group. RNA sequencing was performed at the Beijing Genomics Institute (China). A heatmap illustrating gene expression levels across various samples was generated using the Heatmap software (v1.0.8). Briefly, differential expression analysis was conducted with DESeq2 (v1.4.5), applying a significance threshold of Q value ≤ 0.05. To further explore phenotypic alterations, gene ontology and Kyoto Encyclopedia of Genes and Genomes (KEGG) enrichment analyses were carried out on the differentially expressed genes (DEGs) using the Phyper software, which employs hypergeometric tests. The significance levels of the enriched terms and pathways were adjusted using the Bonferroni correction method, with a stringent cutoff of Q value ≤ 0.05.

2.12. Quantitative real-time PCR analysis

Total RNA was isolated from MC3T3-E1 cells or bone tissues using TRIzol reagent. Complementary DNA was synthesized with a reverse transcription kit (Invitrogen, US) following the manufacturer's protocol. Gene expression levels were quantified through real-time quantitative polymerase chain reaction (RT-PCR). The mRNA expression in each sample was normalized to the expression of the *GAPDH* gene. All experiments were conducted in triplicate. The specific primer sequences used for both cells and tissues are listed in Table S1 of the Supporting information.

2.13. Model of rat skull defect and canine orbital wall bone defect

The animals used in the experiments were obtained from the Hubei Provincial Center for Disease Control and Prevention (China). All procedures involving animals were carried out in compliance with protocols approved by the Chinese National Committee for the Protection and Utilization of Institutional Animals (QR-ADM-G004-4.0). Prior to the procedure, the animals were anesthetized through intraperitoneal injection of pentobarbital (3.5 mg/100 g). An area of approximately 2 cm^2 on the scalp was disinfected with alcohol to define the anatomical site.

A total of thirty 7-week-old, male Sprague-Dawley rats weighing approximately 250 g were selected for skull defects. Skull defects were induced with an orthopedic ring drill with a diameter of 5 mm. Subsequently, all rats were randomly assigned to one of three groups: Control group (n=10), HAMMA/HAP group (n=10), and HAMMA/HAP/BMP-2 group (n=10).

Three 12-month-old, male beagle dogs of similar weight were used. Incisions were made along the inner canthus and lower orbital margins of the left and right eyes to separate the periosteum. Following the separation of the periosteum, the inner wall of the orbit was exposed without

performing enucleation of the eyeball. A ring drill was employed to create an orbital wall defect with a diameter of 10 mm, and approximately 5 mm of surrounding periosteum and ethmoid mucosa were removed. Animal bone defects on the eyes were then implanted with the following composite scaffolds: Control group (left eye; n=3) and HAMMA/HAP/BMP-2 (right eye; n=3) group.

2.14. Micro-computed tomography

The rats and canines were sacrificed at a specified time point after the operation and fixed for 24 h. Subsequently, the samples were scanned using a SkyScan 1176 micro-computed tomography (micro-CT) system (Bruker, Belgium), utilizing a monochromatic beam with 30 keV energy and a resolution of 18 μm. The images and data obtained were processed using CTVox and CTAn software, respectively, and voxels were extracted with a gray value of 130.

2.15. Histological analysis

After micro-CT scanning, the specimens were embedded in paraffin and sectioned at a thickness of 7 μm. All sections were subsequently stained with hematoxylin and eosin (H&E; Sigma-Aldrich, US) and Masson's trichrome (Sigma-Aldrich, US). H&E staining was employed to evaluate the overall tissue architecture and morphology, including cellular distribution and organization.

2.16. Immunofluorescence staining

The immunofluorescence staining protocol involved dewaxing of paraffin-embedded sections, retrieving antigen using an appropriate solution, heating at 95–100°C, and blocking with 5% goat serum for 30 min. Sections were then incubated with the following primary antibodies (all purchased from Proteintech, US) diluted in blocking buffer: OPN polyclonal antibody (1:50; 22952-1-AP), osteocalcin (OCN) polyclonal antibody (1:200; 23418-1-AP), and cluster of differentiation (CD)31 antibody (1:800, 11265-1-AP). Subsequently, samples were incubated with secondary antibodies Cy3-conjugated AffiniPure goat anti-rabbit IgG (H+L; SA00009-2, Proteintech, US) and FITC-conjugated AffiniPure goat anti-rabbit IgG (H+L; SA00003-2, Proteintech, US) diluted in 1% bovine serum albumin/PBS, at 4°C for 24 h. After three washes, fixed cell samples were counterstained with DAPI.

2.17. Statistical analysis

Statistical analyses were conducted using SPSS 18 (IBM, US). All data are presented as mean ± standard deviation. For multiple comparisons in the *in vivo* studies, a one-way analysis of variance was used. Comparisons between two groups were performed using paired t-tests. A p-value of less than 0.05 was considered statistically significant.

3. Results

3.1. Characterization of HAMMA composite scaffolds

The hydrogel scaffold possessed a solid structure at room temperature (Figure 1A). The XRD spectra (Figure 1B) showed that the nano-apatite exhibited characteristic diffraction peaks at 2θ=25°, 31.4°, 32.1°, 32.7°, 39.4°, 46.2°, 53.1°, and 64.1°—a result in accordance with the standard card of HAP (JCPDS-09-0432). However, the characteristic peak of HAP was evident in the hydrogel scaffold, with peak positions similar to those of the standard card of HAP, suggesting that the double crosslinking method did not disrupt the crystalline structure of HAP. The FTIR spectra (Figure 1C) revealed characteristic absorption peaks corresponding to gelatin, specifically the amide I band (C=O stretching vibration) at 1627 cm^{-1}, the amide II band (N–H bending vibration) at 1521 cm^{-1}, and the amide III band (C–N stretching vibration) at 1234 cm^{-1}. The characteristic absorption peaks of (HAP) included the stretching vibration peak of PO_4^{3-} at 1024 and 965 cm^{-1}, the deformation vibration peaks of PO_4^{3-} at 603 and 555 cm^{-1}, the OH stretching vibration peak at 3600 cm^{-1}, and the bending vibration peak at 633 cm^{-1}. Following the addition of HAP to the hydrogel scaffold, the characteristic peaks of HAP appeared at 603 and 555 cm^{-1}, while the O–H peak shifted to 3277 cm^{-1} with a notable increase in width. The peak at 1627 cm^{-1} (amide I band) exhibited a significant broadening, and the peak at 1521 cm^{-1} (amide II band) shifted to 1550 cm^{-1}, confirming the interaction and formation of hydrogen bonds. The SEM morphology of the composite hydrogel is illustrated in Figure 1D. The incorporation of HAP particles did not change the porous network structure of the hydrogel, and the pore size ranged from 500 to 800 μM. The energy spectrum analysis revealed that the HAP particles were uniformly distributed and dispersed (Figure 1E).

The compressive modulus of the hydrogel was determined from the linear region (0–10% strain) of the stress–strain curve. As illustrated in Figure 1F, the elastic modulus of the pure hydrogel without HAP was 3.18 ± 0.09 kPa. The incorporation of HAP particles as reinforcing fillers led to a notable enhancement in the mechanical strength of the hydrogel, accompanied by a considerable increase in the elastic modulus. Moreover, the hydrogel exhibited favorable tensile and bending resistance. In a dry state, the hydrogel could withstand 50 g of weight (Figure 1G). Figure 1H illustrates the water absorption rate of the hydrogels at various time points. All hydrogels exhibited rapid water absorption during the initial hour, with swelling curves demonstrating a gradual increase over time. The addition of HAP particles resulted in a reduction in both the swelling rate and the ultimate water absorption

capacity of the scaffolds, consequently improving their dimensional stability (Figure 1I). In addition, the degradation rates of different composite hydrogels indicated that the pure hydrogel group exhibited the highest weight loss rate, reaching 100% on day 5, indicative of complete degradation (Figure 1J). The incorporation of HAP particles resulted in a notable reduction in the degradation rate of hydrogel scaffolds. The *in vitro* drug release profiles demonstrated that the hydrogel scaffolds were capable of releasing BMP-2 in a continuous manner. On day 7, BMP-2 was released explosively, followed by a gradual flattening of the release profile (Figure 1K). These results demonstrate that the hydrogel scaffolds possess the capacity to load and release drugs.

3.2. *In vitro* biocompatibility and osteogenesis evaluation

As shown in Figure 2A, CCK-8 assay results indicated that HAMMA/HAP/BMP-2 consistently enhanced cellular activity over time. After 1 and 5 days of incubation, cells in each group were stained using a Calcein/PI kit and examined under an inverted fluorescence microscope. The green fluorescence revealed that the cells in each group were evenly distributed and exhibited a polygonal morphology (Figure 2B). In the scratch experiment, the migration speed of cells in HAMMA/HAP/BMP-2 was obviously accelerated, and the scratch area was completely closed within 48 h (Figure 2C). The results of nuclear membrane staining showed that the cells also exhibited a fully extended polygonal structure with no discernible alteration in morphology, which is consistent with the results of the cell viability test, indicating that the hydrogel scaffolds have no obvious cytotoxicity (Figure 2D).

The results of ALP staining (Figure 2E) showed that HAMMA/HAP/BMP-2–treated cells showed a strong blue–purple color compared with the control, indicating that HAMMA/HAP/BMP-2 composite scaffolds result in enhanced ALP activity. Alizarin red staining (Figure 2F) results showed that compared with the control group, HAMMA/HAP composite scaffolds-treated cells had more obvious mineralized nodules and were densely arranged. With the introduction of BMP-2, the extent of red deposition was enhanced, accompanied by more pronounced mineralization nodule formation. COL I, an extracellular matrix protein, promotes osteoblast adhesion and differentiation. OPN, a non-collagenous protein abundantly present in the bone matrix and secreted by osteoblasts, stimulates osteoclast formation and enhances the resorptive activity of mature osteoclasts. Runx2 regulates the phenotype of osteoblasts and the expression of osteoblast-specific matrix proteins, including ALP, COL I, and OPN, ultimately stimulating bone nodule mineralization. Compared to the control group, the expression of osteogenesis-related proteins and factors, such as COL I, OPN, and Runx2, was significantly higher in the group treated with the HAMMA/HAP hydrogel scaffold (Figure 3G & 3H). When the cells were treated with the HAMMA/HAP/BMP-2 hydrogel scaffold, these expressions were further increased.

3.3. *In vitro* osteogenesis mechanism

Following *in vitro* analyses, the molecular mechanisms underlying the effects of HAMMA composite scaffold treatment on MC3T3-E1 cells were determined through RNA sequencing. A total of 2387 DEGs, including 2003 upregulated and 984 downregulated genes, were identified between the HAMMA/HAP composite scaffolds and control groups (Figure S1A & S1C). A total of 2413 DEGs, including 1501 upregulated and 912 downregulated genes, were identified between the HAMMA/HAP/BMP-2 composite scaffolds and control groups (Figure S1B & S1D).

The KEGG pathway analysis was performed to identify signaling pathways that showed significant enrichment among the DEGs when comparing the HAMMA/HAP or HAMMA/HAP/BMP-2 groups with the control group (Figure 3A & 3B). The results demonstrated that osteogenesis-related signaling pathways, such as the mitogen-activated protein kinase (MAPK) signaling pathway, phosphatidylinositol 3-kinase–protein kinase B signaling pathway, calcium signaling pathway, Ras-related protein 1 signaling pathway, and cGMP–protein kinase G signaling pathway, were enriched. The DEGs between the HAMMA/HAP/BMP-2 group and the control group had two additional signaling pathways—the FoxO signaling pathway and the ATP-binding cassette transporters. The protein–protein interaction network analysis of DEGs between the HAMMA/HAP or HAMMA/HAP/BMP-2 group and the control group (Figure 3C & 3D) was performed. The results demonstrated that the osteogenesis-related gene network center included *Fgfr2*, *Fgfr3*, *Fgf18*, *Pik3r3*, *Egf*, *Igf1*, and *Irs1*. To further explore the osteogenesis mechanism, the KEGG pathway results between the HAMMA/HAP group and the HAMMA/HAP/BMP-2 group (Figure 3E) revealed interleukin-17, MAPK, and vascular endothelial growth factor (VEGF) signaling pathways. The protein–protein interaction network analysis of DEGs between the HAMMA/HAP group and HAMMA/HAP/BMP-2 group (Figure 3F) was further performed, demonstrating that the osteogenesis-related gene network center comprised *Fgfr2*, *Fgfr3*, *Pik3r3*, *Egf*, *Igf1*, *Irs1*, *Tgfbr1*, *Smad9*, and *Bmpr1a*.

The differentially expressed proteins and genes in interaction networks were further validated through molecular biology techniques. The RT-PCR analysis

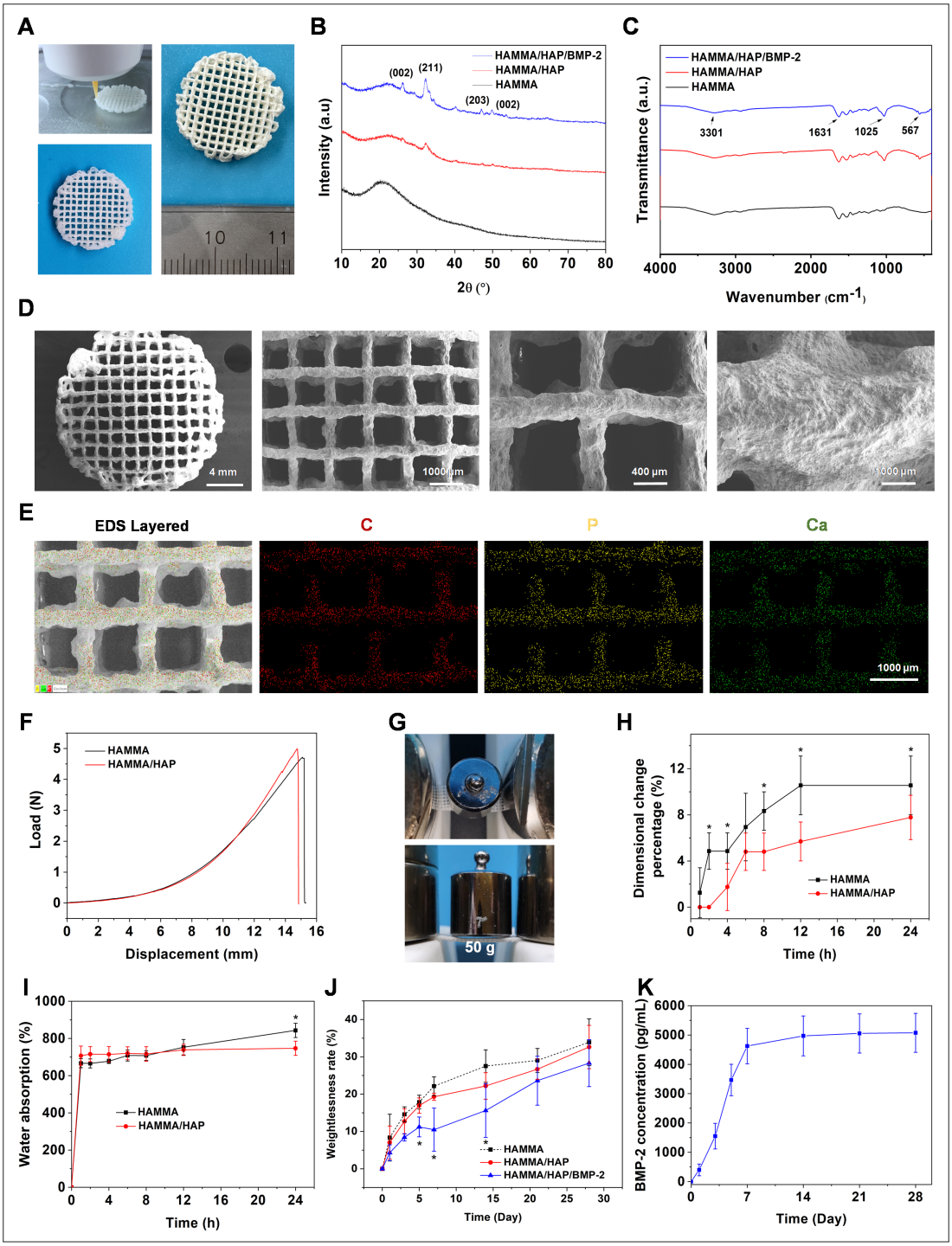

Figure 1. Characterization of HAMMA composite scaffolds. (A) The optical photographs of HAMMA/HAP/BMP-2. The (B) X-ray diffractometry spectra and (C) Fourier transform infrared spectra of HAMMA, HAMMA/HAP, and HAMMA/HAP/BMP-2. (D) The microstructure of HAMMA/HAP/BMP-2. Scale bars (from left to right): 4 mm, 1000, 400, and 1000 μm; magnifications (from left to right): × 6, × 20, × 50, × 200. (E) The element distribution of C, P, and Ca in HAMMA/HAP/BMP-2. Scale bar: 1000 μm; magnification: × 30. The element distribution of HAMMA, HAMMA/HAP, and HAMMA/HAP/BMP-2. (F) The tensile mechanical properties of HAMMA and HAMMA/HAP. (G) Bending performance test of HAMMA (or HAMMA/HAP). The (H) morphological diagram and (I) water absorption rates of materials immersed in water over different durations. (J) The weightlessness rate of HAMMA, HAMMA/HAP, and HAMMA/HAP/BMP-2. (K) The release kinetics of BMP-2 from HAMMA/HAP/BMP-2 composite scaffolds. Notes: n=3; *$p < 0.05$ compared to HAMMA. Abbreviations: BMP-2, bone morphogenetic protein 2; HAMMA, methacrylate-functionalized human acellular amniotic membrane matrix; HAP, hydroxyapatite.

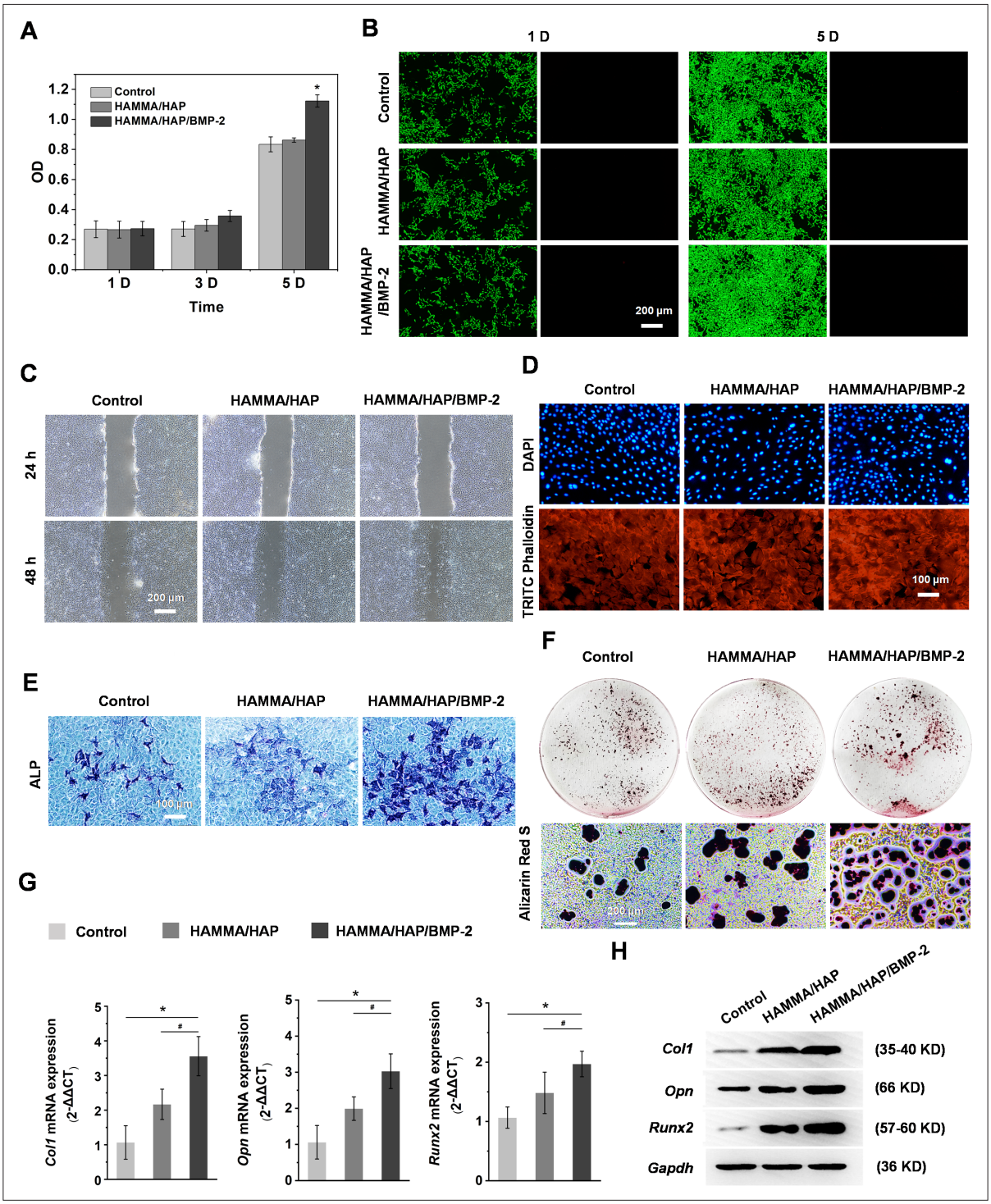

Figure 2. Effect of HAMMA composite scaffolds on biocompatibility and osteogenic differentiation. (A) CCK-8 is used for cell viability determination. (B) The viability of MC3T3-E1 cells *in vitro* was assessed via the Calcein/PI Kit. Scale bar: 200 μm; magnification: ×40. (C) The migration speed of cells in HAMMA/HAP and HAMMA/HAP/BMP-2. Scale bar: 200 μm; magnification: ×40 . (D) The morphology staining of the MC3T3-E1 cells was assessed via nuclear membrane staining. 100 μm; magnification: ×100. (E) The ALP staining of the MC3T3-E1 on day 7. Scale bar: 100 μm; magnification: × 100. (F) Alizarin red S staining of MC3T3-E1 cells on day 14. Scale bar: 200 μm; magnification: × 40. (G & H) Real-time quantitative polymerase chain reaction and Western blotting analysis to assess the expression of osteogenic proteins, including Runx-2, collagen type I, and OPN. Notes: n=3; $^*p < 0.05$ compared to controls; $\#p < 0.05$ compared to HAMMA/HAP. Abbreviations: ALP, alkaline phosphatase; BMP-2, bone morphogenetic protein 2; HAMMA, methacrylate-functionalized human acellular amniotic membrane matrix; HAP, hydroxyapatite; OPN, osteopontin.

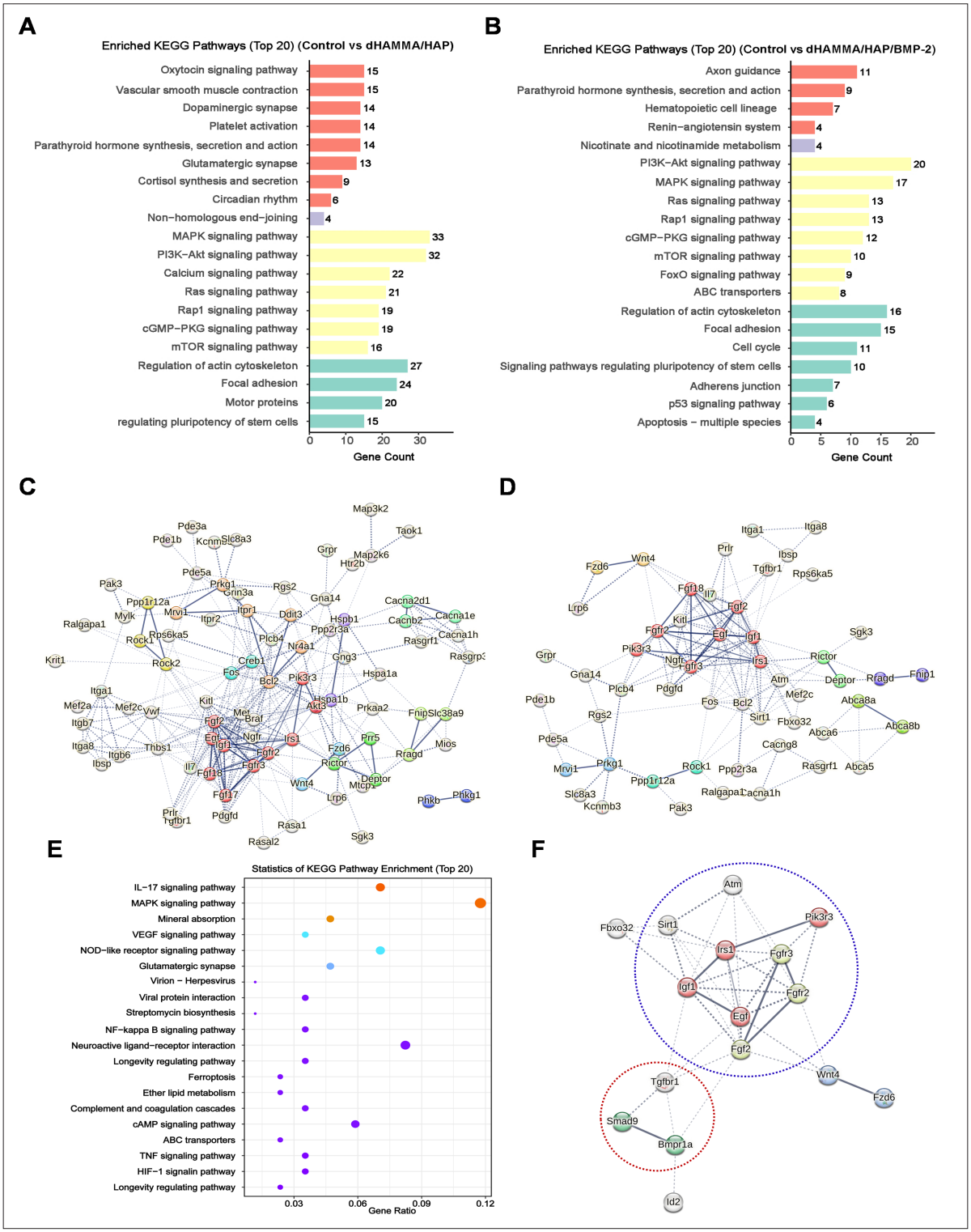

Figure 3. Potential osteogenesis mechanisms of HAMMA composite scaffolds. KEGG pathway enrichment analysis of DEGs (A) between the control and HAMMA/HAP groups; and (B) between the control and HAMMA/HAP/BMP-2 groups. Protein–protein interaction network of DEGs (C) between the control and HAMMA/HAP groups; and (D) between the control and HAMMA/HAP/BMP-2 groups. (E) KEGG pathway enrichment analysis and (F) protein–protein interaction network of DEGs between the HAMMA/HAP and HAMMA/HAP/BMP-2 groups. Abbreviations: BMP-2, bone morphogenetic protein 2; DEG, differentially expressed gene; HAMMA, methacrylate-functionalized human acellular amniotic membrane matrix; HAP, hydroxyapatite; KEGG, Kyoto Encyclopedia of Genes and Genomes.

showed that the DEGs *Fgfr2* (Figure 4A), *Fgfr3* (Figure 4B), *Bmpr1a* (Figure 4C), *Smad9* (**Figure 4D**), and *Wnt4* (**Figure S3A**) were upregulated in the HAMMA/HAP/BMP-2 group. These genes were mainly involved in BMP-2 signaling pathways. Meanwhile, the DEGs *Irs1* (Figure 4E), *Tgfbr1* (Figure 4F), *Fbox32* (Figure 4G), *Sirt1* (Figure 4H), and *Atm* (Figure S3B) were upregulated in the HAMMA/HAP and HAMMA/HAP/BMP-2 groups. These genes were mainly involved in the VEGF signaling pathway. The Western blotting analysis also showed that the expression of proteins insulin receptor substrate 1 (IRS1), fibroblast growth factor receptor 2 (FGFR2), FGFR3, and bone morphogenetic protein receptor type 1A (BMPR1A) were upregulated in HAMMA/HAP/BMP-2 group, while the expression of protein transforming growth factor beta receptor type 1 (TGFBR1) were upregulated in the HAMMA/HAP and HAMMA/HAP/BMP-2 groups. These results indicate that the HAMMA/HAP/BMP-2 composite promotes the differentiation and proliferation of undifferentiated mesenchymal stem cells into osteoblasts, enhances the differentiation and maturation of osteoblasts, and participates in bone growth and remodeling processes, thereby accelerating the repair of bone defects.

3.4. *In vivo* osteogenesis evaluation

To assess their capacity to stimulate osteogenesis and angiogenesis *in vivo*, HAMMA composite scaffolds were implanted into a 5-mm rat calvarial defect model. Samples were obtained and analyzed at 20 and 60 days after surgery (Figure 5A). Immunofluorescence evaluation of the expression of differential protein (Figure 5B) showed that FGFR3 and BMPR1A were upregulated in the HAMMA/HAP/BMP-2 group, and FGFR2 was upregulated in the HAMMA/HAP and HAMMA/HAP/BMP-2 groups (Figure 5C–E). These *in vivo* results were similar to those of the *in vitro*.

The degradation of the HAMMA composite scaffolds was accompanied by the ingrowth of new bone tissues, as revealed in 3D images reconstructed using micro-CT software. Furthermore, bone formation was detected to be higher in the HAMMA/HAP/BMP-2 group than in the control group at 60 days after implantation (Figure 6A). The regenerated bone volumes at the implantation sites of the three samples were also calculated separately to evaluate bone regeneration more accurately (Figures 6B & S4B). The control group exhibited a mean value of 6.21 ± 2.1%, while the HAMMA/HAP group demonstrated a mean value of 13.7 ± 6.33%. In contrast, the HAMMA/HAP/BMP-2 group exhibited the highest mean value of 24.64 ± 9.30%. Histological analysis was applied to provide detailed observations of osteogenesis and angiogenesis in the HAMMA/HAP and HAMMA/HAP/BMP-2 groups at 60 days (Figure 6C). H&E staining and Masson trichrome staining further revealed that all HAMMA composite scaffolds were absorbed gradually after implantation into the bone defect. In contrast, new bone tissues and blood vessels containing murine erythrocytes were formed around HAMMA/HAP and HAMMA/HAP/BMP-2. Obviously, more trabecular bones and blood vessels were observed in the HAMMA/HAP/BMP-2–treated implant than others.

The immunohistochemical analysis revealed that the expression levels of CD31, OPN, and OCN surrounding the HAMMA/HAP/BMP-2 implants at 60 days were significantly higher compared to those in the HAMMA/HAP and control groups (Figure 7), suggesting that VEGF produced by cells in bone could stimulate the formation of new blood vessels. Additionally, the staining results for OPN and OCN revealed significantly higher bone formation activity in the HAMMA/HAP/BMP-2 group compared to both the HAMMA/HAP and control groups at weeks 4 and 8.

3.5. *In vivo* therapeutic efficacy of orbital bone defects

Our results have shown that HAMMA/HAP/BMP-2 could induce faster bone formation and maturation in a rat full-thickness skull defect. However, the size and location of the defect were the main determinants of the innate ability of bone healing. In particular, the bone of the orbital wall was thin, the adjacent bone contained fewer mesenchymal stem cells, and its proximity to the paranasal sinuses resulted in a poor blood supply. Therefore, we conducted a second *in vivo* study to evaluate the potential application of HAMMA/HAP/BMP-2 in canine orbital wall bone defect, which is considered a severe test for bone implantation (Figures 8A, 8B, & S5).

The entire canine cranium, including the orbital bone defects, was scanned and reconstructed in 3D via micro-CT post-treatment. As depicted in **Figure 8C**, 90 days after implantation, the blank control group showed significant bone defects at the infraorbital margin of the orbital bone fractures, with the implanted material having completely degraded. Conversely, an increase in bone mineral density was observed, indicative of neoplastic bone tissue growth. A quantitative analysis was performed on the reconstructed 3D models derived from micro-CT imaging, and the bone volume/total volume (BV/TV) values were calculated for each group of samples. The results in Figure S6 depict a significant increase in the BV/TV value of the HAMMA/HAP/BMP-2 group (11.37 ± 2.93%) after 90 days of implantation compared to the control group (32.06 ± 3.76%).

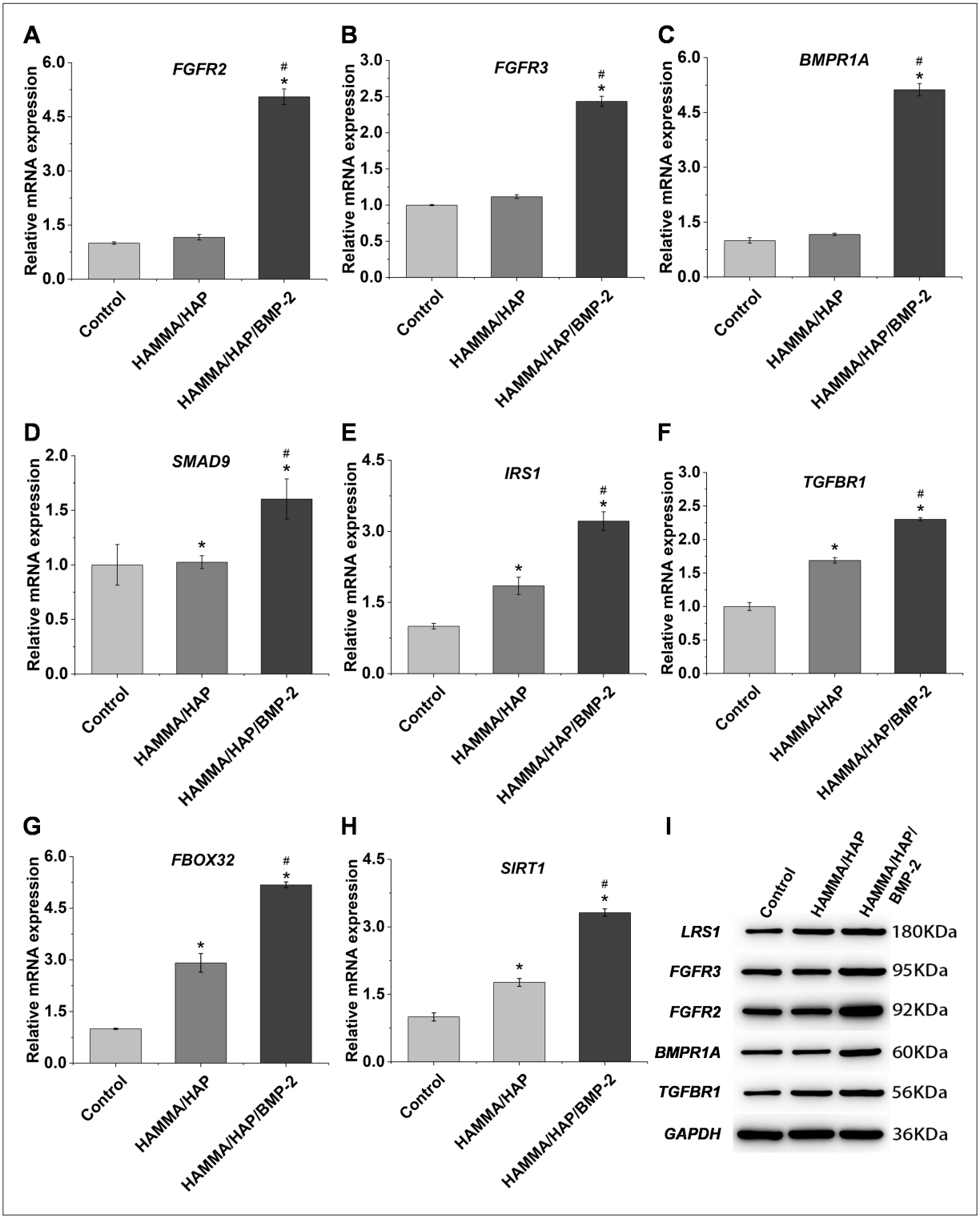

Figure 4. Verification of differentially expressed genes and proteins in interaction networks. RT-PCR analysis to assess the expression of differentially expressed genes: (A) *FgFr2*, (B) *FgFr3*, (C) *Bmpr1a*, (D) *Smad9*, (E) *Irs1*, (F) *Tgfbr1*, (G) *Fbox32*, and (H) *Sirt1*. (I) Western blotting analysis to assess the expression of differentially expressed proteins, IRS1, FGFR2, FGFR3, BMPR1A, and TGFBR1. Notes: n=3; *$p < 0.05$ compared to control; #$p < 0.05$ compared to HAMMA/HAP. Abbreviations: BMP-2, bone morphogenetic protein 2; BMPR1A, bone morphogenetic protein receptor type 1A; FGFR2/3, fibroblast growth factor receptor 2/3; GAPDH, glyceraldehyde-3-phosphate dehydrogenase; HAMMA, methacrylate-functionalized human acellular amniotic membrane matrix; HAP, hydroxyapatite; IRS1, insulin receptor substrate 1; TGFBR1, transforming growth factor beta receptor type 1.

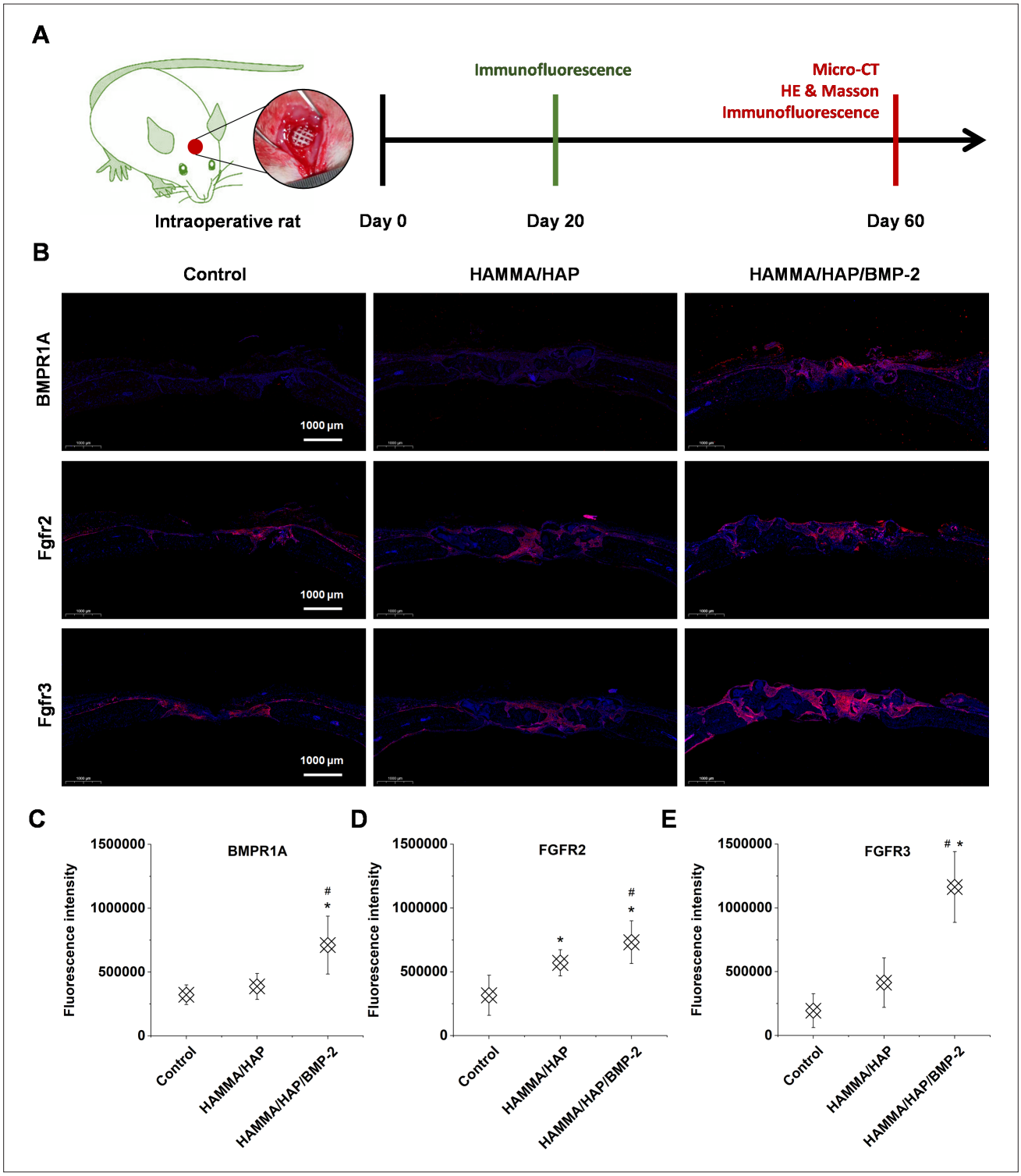

Figure 5. *In vivo* study of HAMMA composite scaffolds in the treatment of rat calvarial defect. (A) Establishment of rat calvarial defect and implantation of scaffolds. (B) Immunofluorescence evaluation of the expression of proteins under different treatments after 20 days. Scale bars: 1000 μm; magnifications: × 4. (C–E) Statistics of immunofluorescence intensity from differentially expressed proteins. Notes: n=3; *$p < 0.05$ compared to control; #$p < 0.05$ compared to HAMMA/HAP. Abbreviations: BMP-2, bone morphogenetic protein 2; BMPR1A, bone morphogenetic protein receptor type 1A; FGFR2/3, fibroblast growth factor receptor 2/3; HAMMA, methacrylate-functionalized human acellular amniotic membrane matrix; HAP, hydroxyapatite; HE, hematoxylin and eosin.

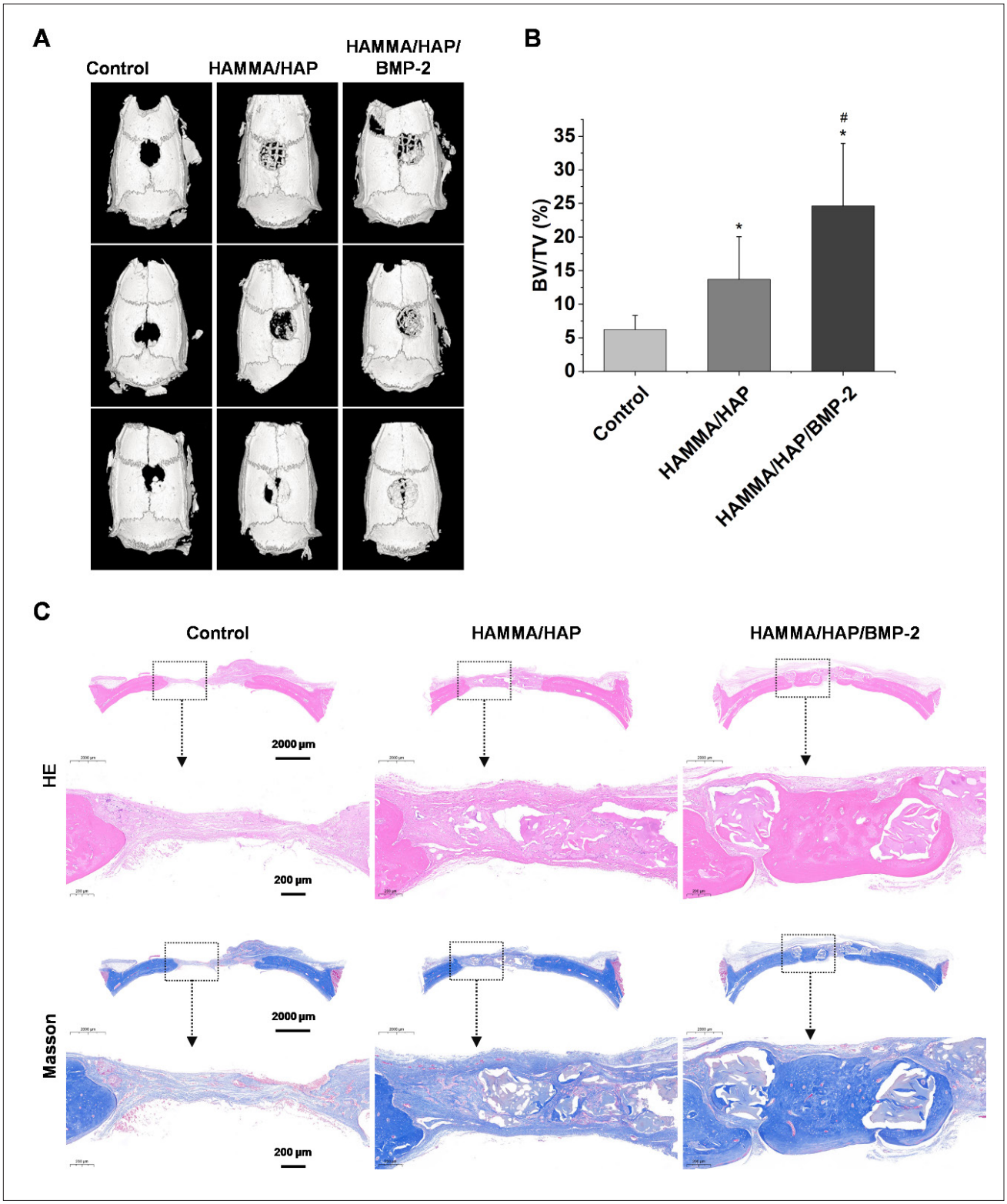

Figure 6. Regeneration of bone defects in rats. (A) Representative micro-CT reconstruction images in coronal and sagittal views in different groups at 60 days post-surgery. (B) Micro-CT quantification of the calvarial defects. (C) HE and MT staining of the calvarial defects. Scale bars: 2000 μm (top), 200 μm (bottom); magnifications: × 4 (top), ×40 (bottom). Notes: n=3; *p < 0.05 compared to control; #p < 0.05 compared to HAMMA/HAP. Abbreviations: BMP-2, bone morphogenetic protein 2; BV/TV, bone volume/total volume; CT, computed tomography; HAMMA, methacrylate-functionalized human acellular amniotic membrane matrix; HAP, hydroxyapatite; HE, hematoxylin and eosin; MT, Masson's trichrome.

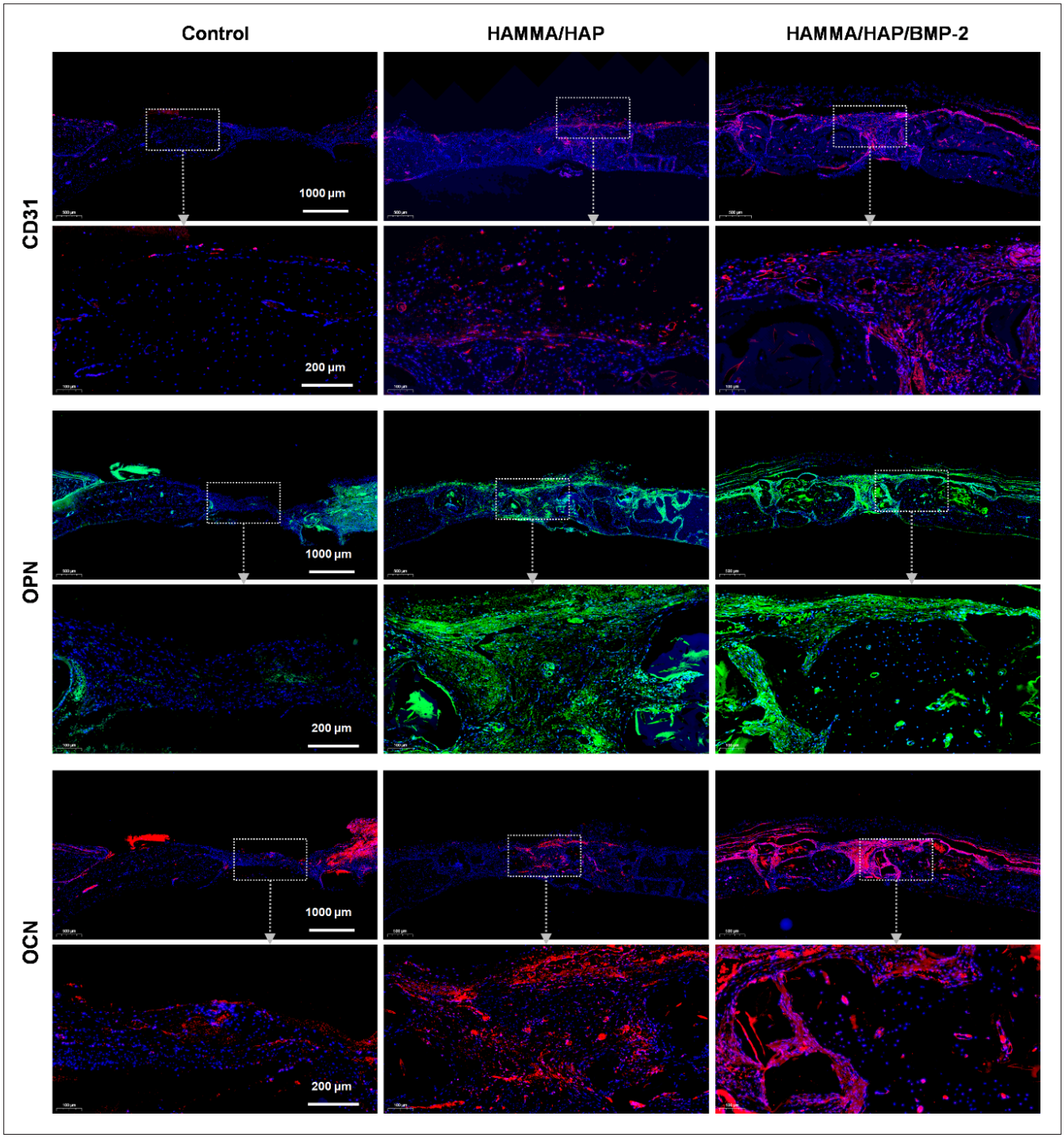

Figure 7. Co-staining of CD31 (red), OPN (green), OCN (red), and DAPI (nucleus, blue) in specimens from the calvarial defects. Scale bars: 1000 μm (top), 200 μm (bottom); magnifications: ×4 (top), ×40 (bottom). Abbreviations: BMP-2, bone morphogenetic protein 2; CD31, cluster of differentiation 31; DAPI, 4',6-Diamidino-2-phenylindole; HAMMA, methacrylate-functionalized human acellular amniotic membrane matrix; HAP, hydroxyapatite; OCN, osteocalcin; OPN, osteopontin.

After 90 days of implantation, histological sections of the samples were subjected to H&E and Masson's trichrome staining, with the results presented in Figure 8D. In the control group, only a little orbital bone tissue growth was observed in the area of the orbital bone defect. However, part of the mucosa of the ethmoid sinus was completely repaired, and a small amount of paperboard bone fragments of ethmoid bone were observed to be growing towards the central area. In the scaffold groups, the scaffolds were fully degraded. New bone tissues appeared light red and light blue, while mature bone tissues were stained red and blue. Immunofluorescence staining for OCN (red) and OPN (green) in different scaffold groups is presented in Figure 8E. The OCN and OPN fluorescence intensity in the HAMMA/HAP/BMP-2 group was significantly enhanced than the control groups, demonstrating that the bone formation activity of the HAMMA/HAP/BMP-2 group was stronger than the control groups.

4. Discussion

The bone of the orbital wall is structurally fragile and susceptible to fracture and collapse in the presence of external force. Most of the bone defect areas after fracture are typically covered by fibrous mucosal tissues, which are often ineffective in restoring the mechanical properties of the original bony orbital wall. Consequently, enophthalmos or displacement, diplopia, and eye movement disorders may arise, as well as potential visual loss or decline. The current surgical treatment strategies primarily entail the repair of orbital soft tissues and subsequent bridging of the bone wall defects with artificial materials.[17] However, the complex geometry of the orbital bones, their limited thickness, and the intricate interface between bone and biomaterials pose considerable challenges in the development of porous bioactive scaffolds for repairing orbital bone defects. Research on the application of porous biological scaffolds in thin-walled bone tissue is still limited. In recent years, 3D printing technology has been employed to fabricate bone implants with internal pores and external geometry conforming to the specific requirements of personalized orbital fractures.[18] In this study, HAMMA composite scaffolds featuring controlled micromorphological and microstructural parameters were successfully fabricated via 3D printing technology and subsequently applied in the reconstruction of orbital bone defects.

The FTIR results indicate that the hydrogel scaffolds are formed through a combination of physical (hydrogen bonding) and chemical crosslinking (photocrosslinking), ensuring both material uniformity and strong adhesion. XRD results indicate that the double crosslinking approach does not disrupt the crystalline structure of HAP, which could be attributed to the elevated surface energy of HAP. In order to maintain the structural stability of porous scaffolds during bone growth repair, it is necessary to provide mechanical support to the defect area. Our results showed that the HAMMA/HAP scaffold exhibited a higher tensile strength than the pure HAMMA scaffold. In addition, the final water absorption of the scaffold was observed to be lower than that of the pure HAMMA scaffold. These findings suggest that HAP-doped scaffolds are superior to pure HAMMA scaffolds in terms of mechanical strength and dimensional stability.

Although the incorporation of HAP reduces the internal space of the hydrogel, it significantly influences the crosslinking density, which was observed to be closely associated with the swelling ratio. A higher crosslinking degree results in reduced swelling capacity and improved dimensional stability. The relatively low swelling ability of these hydrogels may promote the exchange of nutrients and metabolic waste within the hydrogel matrix, as well as cell encapsulation and cell survival, by reducing the likelihood of water molecules entering the hydrogels.[19] In contrast, biodegradation represents another important factor of biological scaffolds. HAP can act as a noncovalent cross-linker between polymer chains, effectively increasing the overall molecular weight of the polymer network and thereby significantly improving the cohesive strength of the adhesive. Consequently, the degradation rate is found to decrease significantly with an increase in HAP particle content.[20]

The physical properties of hydrogel scaffolds, including stability, capacity to transport nutrients, drug release time, and their biological properties that promote cell adhesion, metabolism, and new bone regeneration, are significantly affected by their swelling and degradation properties.[21–23] An acellular scaffold exhibiting superior hydrophilic properties was employed as a carrier for the incorporation of BMP-2. BMP-2 and the hydrogel were combined through hydrogen bonding, which prolonged the drug release time. Studies have shown that the initial burst release of BMP-2 can activate downstream signaling pathways, such as BMP/mothers against decapentaplegic homolog (SMAD) and MAPK pathways, more strongly, thus significantly promoting early osteogenic differentiation.[24] Furthermore, the addition of inorganic nanoHAP particles with reduced hydrophilicity leads to the formation of mutual bonding between the raw materials and nanoHAP, resulting in a reduction in the internal pore size of the hydrogel scaffold, an increase in the density of internal structure, and an enlargement of the pore wall thickness. Thereafter, this reduction in the free passage space available to water molecules leads to decreased equilibrium swelling and slower degradation rates. As a result, the release of BMP-2

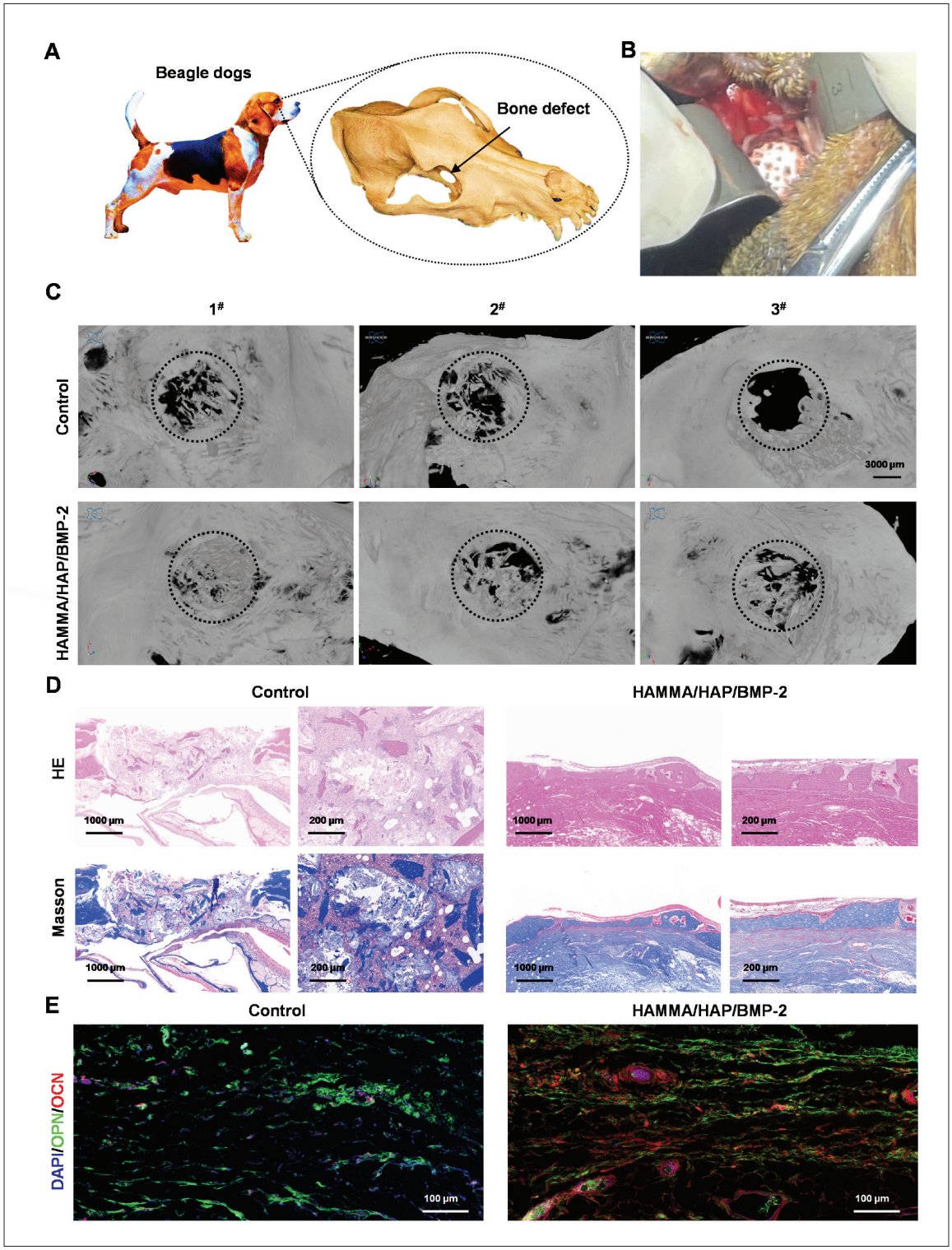

Figure 8. *In vivo* study of HAMMA composite scaffolds in the treatment of orbital bone defects. (A, B) Establishment of orbital bone defects and the implantation of scaffolds. (C) Representative micro-CT reconstruction images in the control and scaffolds groups at 90 days post-surgery. Scale bar: 500 μm; magnification: ×4 . (D) HE and MT staining of orbital bone defects. Scale bars: 1000 or 200 μm; magnifications:×4 or × 40. (E) Immunofluorescence of the osteogenic proteins. Scale bars: 100 μm; magnifications: × 100. Abbreviations: BMP-2, bone morphogenetic protein 2; CD31, cluster of differentiation 31; DAPI, 4',6-diamidino-2-phenylindole; HAMMA, methacrylate-functionalized human acellular amniotic membrane matrix; HAP, hydroxyapatite; HE, hematoxylin and eosin; OCN, osteocalcin; OPN, osteopontin.

can be effectively regulated, maintaining a therapeutically effective drug concentration within the bone defect area. This controlled release helps modulate the immune microenvironment during the early stages of bone repair, promotes the recruitment of osteoblasts, and accelerates the healing of bone defects.[25,26]

The BMP-2 protein can regulate bone metabolism through the classical BMP/SMAD pathway and non-classical MAPK pathway.[27] In a non-canonical mechanism, BMP-2 rapidly activates the transforming growth factor-beta activated kinase (TAK)1/2–mitogen-activated protein kinase (MAPK)1/2–extracellular signal-regulated kinase (ERK)1/2 signaling pathway by recruiting the TAK1-binding protein 1–TAK1 complex via BMPR1A. This activation modulates the expression of target genes and influences osteogenic differentiation.[28] Meanwhile, Wnt signaling upregulates the expression of Runx transcription factor family genes, promotes early differentiation of mesenchymal stem cells, and suppresses their late apoptosis, thereby facilitating osteogenic differentiation.[29] Cell signal pathways are interconnected to form a complex network to accurately regulate the differentiation process. *Jag1*, one of the target genes of the Wnt classical pathway in osteoblasts, encodes a protein that is an important ligand of the Notch signaling pathway, thus becoming an important node associated with Notch and Wnt pathways, whereas the Wnt pathway is also regulated by other signaling pathways. During the activation process of the Wnt pathway, calcium channels need to be opened, protein kinase C (PKC)/ERK needs to be involved, and calcium channel proteins need to be sulfhydrylated at specific cysteine sites to play a biological role.[30] As the enhanced activity of a calcium peak initiated by HAP nanorods leads to the activation of c-Jun and thus suppresses the expression of gamma-aminobutyric acid (GABA)ergic/glutamatergic selection gene *TLX3*, HAP may activate calcium channels during the activation process of the Wnt pathway.[31]

The HAM is a natural, acellular extracellular matrix material enriched with a variety of bioactive factors. It has been extensively utilized in skin and ocular surface tissue engineering to promote tissue regeneration. However, its application in bone tissue engineering remains relatively unexplored, mainly owing to the need for further research into its mechanical properties, compatibility with the cellular growth microenvironment, and potential to support bone regeneration. Studies have shown that HAMs, which exhibit excellent biocompatibility, facilitate the proliferation and osteogenic differentiation of bone marrow mesenchymal stem cells. Moreover, they can upregulate the expression of genes related to cell recruitment and bone remodeling, such as *CXCR4*, *MCP1*, *OC*, and *Catk*.[32] Additionally, BMP-2 has been shown to promote the differentiation and proliferation of undifferentiated mesenchymal stem cells into chondrocytes and osteoblasts, enhance the differentiation and maturation of osteoblasts, play a crucial role in the growth, development, and remodeling of bone and cartilage, and accelerate the repair of bone defects. In this work, BMP-2 was introduced to increase the biological activity of the HAM. *The in vivo* and *in vitro* osteogenesis experiments suggest that BMP-2 has a significant impact on bone regeneration.

Given the unique anatomical location and bone tissue structure of the orbital wall, tissue-engineered bone constructs were used to repair circular, full-thickness bone defects measuring 10 mm in diameter in the medial orbital wall of dogs. This study also explored the feasibility of employing a hydrogel for the reconstruction of orbital wall bone defects. CT imaging revealed that the implanted HAP composite material degraded gradually, and the surrounding bone wall was repaired. In the control group, the degradation was accompanied by only a small amount of new bone formation, thereby maintaining obvious defects. The histological examination clearly revealed the morphology of new bone tissues, which is significant for assessing bone remodeling and new bone metabolism. The strategy employed in this study is not only applicable to orbital bone repair but also provides a transferable research paradigm for tissue engineering of other thin-walled bones, such as cranial vault and jawbones, and even load-bearing bones. HAMMA, as a functionally versatile matrix material, holds promise for application in the regeneration of other tissues such as cartilage and skin through combination with different bioactive factors or inorganic components. It also plays an important theoretical and practical foundation for future research directions in bone tissue engineering, such as personalized treatment, composite biomaterial design, and optimization of vertical bone augmentation.[33]

5. Conclusion

In conclusion, a HAP/BMP-2–mineralized decellularized amniotic membrane scaffold was developed for bone tissue engineering applications. In this study, 10× SBF was used as a simple and easy strategy to modify the amniotic membrane with HAP and BMP-2. The physicochemical properties and biological activity of acellular amniotic membrane matrix composite scaffolds (HAMMA/HAP/BMP-2) were modulated through chemical composition changes combined with advanced 3D printing technology, thus optimizing the macro- and microstructural design of materials. A novel porous scaffold with multiple functions, such as effectively inducing and guiding tissue growth, was successfully prepared, providing an innovative research perspective for the design and preparation of orbital

repair materials. This work addresses the limitations of current clinical orbital repair materials, including those used for repairing orbital bone wall defects and filling orbital prosthesis.

Acknowledgments

None.

Funding

This work was supported by grants from the National Natural Science Foundation of China (32201109), the New Clinical Diagnosis and Treatment Technology and Public Health of Suqian First Hospital (SY202205), and the Basic and Applied Basic Research Foundation of Guangdong Province (2021A1515110557).

Conflict of interest

The authors declare no conflict of interest.

Author contributions

Conceptualization: Bing Qin, Wei Liu
Formal analysis: Yabo Shi, Yi Wang
Investigation: Bing Qin, Yiyi Chen
Methodology: Bing Qin, Yabo Shi
Writing–original draft: Bing Qin, Yi Wang
Writing–review & editing: Wei Liu

Ethics approval and consent to participate

The animals used in the experiments were obtained from the Hubei Provincial Center for Disease Control and Prevention (Wuhan, China). All procedures involving animals were carried out in compliance with protocols approved by the Chinese National Committee for the Protection and Utilization of Institutional Animals (QR-ADM-G004-4.0).

Consent for publication

Not applicable.

Availability of data

Data will be made available upon reasonable request to the corresponding author.

References

1 Sachs ME. Orbital floor fractures: the maxillary approach. *Adv Ophthalmic Plast Reconstr Surg*. 1987;6(1):387-391.

2. Ni X, Feng J, Liang M, *et al*. Enhancing bone repair with β-TCP-based composite scaffolds: a review of design strategies and biological mechanisms. *Orthop Res Rev*. 2025;17:313-340.
doi: 10.2147/ORR.S525959

3. Al-Khdhairi OBH, Abdulrazaq SS. Is orbital floor reconstruction with titanium mesh safe?. *J Craniofac Surg*. 2017;28(7):e692-e694.
doi: 10.1097/SCS.0000000000003896

4. Shah HA, Shipchandler T, Vernon D, *et al*. Extra-ocular movement restriction and diplopia following orbital fracture repair. *Am J Otolaryngol*. 2018;39(1):34-36.
doi: 10.1016/j.amjoto.2017.08.008

5. Kwon H, Kim HJ, Seo BF, Jeong YJ, Jung SN, Shim HS. The role of resorbable plate and artificial bone substitute in reconstruction of large orbital floor defect. *Biomed Res Int*. 2016;2016:1358312.
doi: 10.1155/2016/1358312

6. Song X, Li L, Sun Y, Fan X, Li Z. Long-term infectious complications of using porous polyethylene mesh for orbital fracture reconstruction. *Medicine (Baltimore)*. 2016;95(25):e3819.
doi: 10.1097/MD.0000000000003819

7. Zheng YX, Zhao HY, Jing XB, *et al*. Reconstruction of orbital floor defect with polylacticglycolide acid/recombinant human bone morphogenetic protein 2 compound implanted material in sheep. [in Chinese] *Zhonghua Yan Ke Za Zhi*. 2006;42(6):535-539.

8. Samadikuchaksaraei A, Mehdipour A, Habibi Roudkenar M, *et al*. A dermal equivalent engineered with TGF-β3 expressing bone marrow stromal cells and amniotic membrane: cosmetic healing of full-thickness skin wounds in rats. *Artif Organs*. 2016;40(12):266-279.
doi: 10.1111/aor.12807

9. Zheng Y, Ji S, Wu H, *et al*. Topical administration of cryopreserved living micronized amnion accelerates wound healing in diabetic mice by modulating local microenvironment. *Biomaterials*. 2017;113:56-67.
doi: 10.1016/j.biomaterials.2016.10.031

10. Etchebarne M, Fricain JC, Kerdjoudj H, *et al*. Use of amniotic membrane and its derived products for bone regeneration: a systematic review. *Front Bioeng Biotechnol*. 2021;9:661332.
doi: 10.3389/fbioe.2021.661332

11. Leal-Marin S, Kern T, Hofmann N, *et al*. Human amniotic membrane: a review on tissue engineering, application, and storage. *J Biomed Mater Res B Appl Biomater*. 2021;109(8):1198-1215.
doi: 10.1002/jbm.b.34782

12. Dadkhah Tehrani F, Firouzeh A, Shabani I, Shabani A. A review on modifications of amniotic membrane for biomedical applications. *Front Bioeng Biotechnol*. 2021;8:606982.
doi: 10.3389/fbioe.2020.606982

13. Suter AJ, Molteno AC, Bevin TH, *et al*. Long term follows up of bone derived hydroxyapatite orbital implants. *Br J Ophthalmol*. 2002;86(11):1287-1292.
doi: 10.1136/bjo.86.11.1287

14. Yan S, Feng L, Zhu Q, *et al*. Controlled release of BMP-2 from a Heparin-conjugated strontium-substituted nanohydroxyapatite/silk fibroin scaffold for bone regeneration. *ACS Biomater Sci Eng*. 2018;4(9):3291-3303.
doi: 10.1021/acsbiomaterials.8b00549

15. Dewey MJ, Johnson EM, Slater ST, Milner DJ, Wheeler MB, Harley BAC. Mineralized collagen scaffolds fabricated with amniotic membrane matrix increase osteogenesis under inflammatory conditions. *Regen Biomater*. 2020;7(3):247-258.
doi: 10.1093/rb/rbaa005

16. Jia Z, Ma H, Liu J, *et al*. Preparation and characterization of polylactic acid/nano hydroxyapatite/nano hydroxyapatite/human acellular amniotic membrane (PLA/nHAp/HAAM) hybrid scaffold for bone tissue defect repair. *Materials (Basel)*. 2023;16(5):1937.
doi: 10.3390/ma16051937.

17. Cole P, Boyd V, Banerji S, Hollier LH. Comprehensive management of orbital fractures. *Plast Reconstr Surg*. 2007;120(7 Suppl 2):57S-63S.
doi: 10.1097/01.prs.0000260752.20481.b4

18. Wallace J, Wang M, Thompson P, *et al*. Validating continuous digital light processing (cDLP) additive manufacturing accuracy and tissue engineering utility of a dye-initiator package. *Biofabrication*. 2014;6(1):015003.
doi: 10.1088/1758-5082/6/1/015003

19. Zhong M, Sun J, Wei D, *et al*. Establishing a cell-affinitive interface and spreading space in a 3D hydrogel by introduction of microcarriers and an enzyme. *J Mater Chem B*. 2014;2(38):6601-6610.
doi: 10.1039/c4tb00887a

20. Yang R, Chen B, Zhang X, Bao Z, Yan Q, Luan S. Degradable nanohydroxyapatite-reinforced superglue for rapid bone fixation and promoted osteogenesis. *ACS Nano*. 2024;18(11):8517-8530.
doi: 10.1021/acsnano.4c01214

21. Jamnezhad S, Asefnejad A, Motififard M, *et al*. Development and investigation of novel alginate-hyaluronic acid bone fillers using freeze drying technique for orthopedic field. *Nanomed Res J*. 2020;5(4):306-315.
doi: 10.22034/nmrj.2020.04.001

22. Lakkireddy C, Vishwakarma SK, Bardia A, *et al*. Biofabrication of allogenic bone grafts using cellularized amniotic scaffolds for application in efficient bone healing. *Tissue Cell*. 2021;73:101631.
doi: 10.1016/j.tice.2021.101631

23. Dawiec G, Niemczyk W, Wiench R, Niemczyk S, Skaba D. Introduction to amniotic membranes in maxillofacial surgery-a scoping review. *Medicina (Kaunas)*. 2024;60(4):663.
doi: 10.3390/medicina60040663

24. Han S, Paeng KW, Park S, Jung UW, Cha JK, Hong J. Programmed BMP-2 release from biphasic calcium phosphates for optimal bone regeneration. *Biomaterials*. 2021;272:120785.
doi: 10.1016/j.biomaterials.2021.120785

25. Bölgen N, Plieva F, Galaev I, Mattiasson B, Pişkin E. Cryogelation for preparation of novel biodegradable tissue-engineering scaffolds. *J Biomater Sci Polym Ed*. 2007;18(9):1165-1179.
doi: 10.1163/156856207781554046

26. Xu M, Qin M, Zhang X, *et al*. Porous PVA/SA/HA hydrogels fabricated by dual-crosslinking method for bone tissue engineering. *J Biomater Sci Polym Ed*. 2020;31(6):816-831.
doi: 10.1080/09205063.2020.1720155

27. Dorman LJ, Tucci M, Benghuzzi H. In vitro effects of bmp-2, bmp-7, and bmp-13 on proliferation and differentation of mouse mesenchymal stem cells. *Biomed Sci Instrum*. 2012;48:81-87.

28. Kua HY, Liu H, Leong WF, *et al*. c-Abl promotes osteoblast expansion by differentially regulating canonical and non-canonical BMP pathways and p16INK4a expression. *Nat Cell Biol*. 2012;14(7):727-737.
doi: 10.1038/ncb2528

29. Grassi F, Tyagi AM, Calvert JW, *et al*. Hydrogen sulfide is a novel regulator of bone formation implicated in the bone loss induced by estrogen deficiency. *J Bone Miner Res*. 2016;31(5):949-963.
doi: 10.1002/jbmr.2757

30. Matsumoto Y, Otsuka F, Takano-Narazaki M, *et al*. Estrogen facilitates osteoblast differentiation by upregulating bone morphogenetic protein-4 signaling. *Steroids*. 2013;78(5):513-520.
doi: 10.1016/j.steroids.2013.02.011

31. Shen Y, Liu F, Duan J, *et al*. Biomaterial cues regulated differentiation of neural stem cells into GABAergic neurons through Ca2+/c-Jun/TLX3 signaling promoted by hydroxyapatite nanorods. *Nano Lett*. 2021;21(17):7371-7378.
doi: 10.1021/acs.nanolett.1c02708

32. Tang K, Wu J, Xiong Z, Ji Y, Sun T, Guo X. Human acellular amniotic membrane: a potential osteoinductive biomaterial for bone regeneration. *J Biomater Appl*. 2018;32(6):754-764.
doi: 10.1177/0885328217739753

33. Akhlaghi F, Hesami N, Rad MR, Nazeman P, Fahimipour F, Khojasteh A. Improved bone regeneration through amniotic membrane loaded with buccal fat pad-derived MSCs as an adjuvant in maxillomandibular reconstruction. *J Craniomaxillofac Surg*. 2019;47(8):1266-1273.
doi: 10.1016/j.jcms.2019.03.030